



## OPEN ACCESS

## EDITED BY

Licheng Cao,  
China University of Geosciences Wuhan,  
China

## REVIEWED BY

Chang Liu,  
Texas A and M University, United States  
Hailing Liu,  
Chinese Academy of Sciences (CAS), China

## \*CORRESPONDENCE

Lifeng Zhong

✉ zhonglifeng@sml-zhuhai.cn

RECEIVED 30 May 2024

ACCEPTED 15 July 2024

PUBLISHED 01 August 2024

## CITATION

Cai Z, Wang X, Zhong L, Zhang C and Sui X  
(2024) The sources and transport model of  
deep-sea sediment in the Southwest Sub-  
basin of the South China Sea.  
*Front. Mar. Sci.* 11:1440886.  
doi: 10.3389/fmars.2024.1440886

## COPYRIGHT

© 2024 Cai, Wang, Zhong, Zhang and Sui. This  
is an open-access article distributed under the  
terms of the [Creative Commons Attribution  
License \(CC BY\)](https://creativecommons.org/licenses/by/4.0/). The use, distribution or  
reproduction in other forums is permitted,  
provided the original author(s) and the  
copyright owner(s) are credited and that the  
original publication in this journal is cited, in  
accordance with accepted academic  
practice. No use, distribution or reproduction  
is permitted which does not comply with  
these terms.

# The sources and transport model of deep-sea sediment in the Southwest Sub-basin of the South China Sea

Zhourong Cai<sup>1,2,3</sup>, Xiaoxiang Wang<sup>1,2,3</sup>, Lifeng Zhong<sup>2\*</sup>,  
Cheng Zhang<sup>1,2,3</sup> and Xin Sui<sup>1,2,3</sup>

<sup>1</sup>School of Marine Sciences, Sun Yat-sen University, Zhuhai, China, <sup>2</sup>Southern Marine Science and Engineering Guangdong Laboratory (Zhuhai), Zhuhai, China, <sup>3</sup>Guangdong Provincial Key Laboratory of Marine Resources and Coastal Engineering, Zhuhai, China

Turbidity current deposition belongs to event deposition, which is of great significance to the study of neotectonic movement. However, turbidite deposits are rarely found in deep-sea basins. In this work, the particle size, mineralogy, and geochemistry of 14 deep-sea sediment cores from the Southwest Sub-basin (SWSB) of South China Sea (SCS) and its periphery are used to trace the sources of sediment and reveal the sedimentological and geochemical characteristics of deep-sea sediments. The results show that quartz and feldspar are the main minerals in the core sediments from the SWSB, and there are multiple layers of turbidites. Geochemical analysis reveals that the composition of the core sediments is close to that of the western margin of the SCS and is similar to that of the upper continental crust (UCC) and is inherited from terrigenous sediments. The Sr–Nd isotope results indicate that the sediment provenances of the SWSB are from the Mekong River, Sunda Shelf and Red River, showing the characteristics of multiple sources. Therefore, we propose that terrigenous materials from multiple sources can reach the deep-sea basin of the SWSB, and we also establish a transport model of deep-sea terrigenous sediment. Terrigenous materials were first carried by rivers and surface currents to the continental margins near the SWSB, and fine materials were subsequently transported by surface currents to the deep-sea basin, while coarse materials were subsequently transported by turbidity currents. Turbidity current deposits provide an approach for studying the transport of coarse materials in deep-sea basins of SWSB.

## KEYWORDS

Southwest Sub-basin, South China Sea, sediment sources, transport model, deep-sea sediment

## 1 Introduction

A large amount of terrestrial sediment from the Tibetan Plateau is transported to the Indian Ocean and western Pacific marginal seas due to plateau uplift and the formation and evolution of the western Pacific marginal seas and the Asian monsoon system, which are considered the most important tectonic and climatic events in the Cenozoic (Hall, 2002; Clark et al., 2005). As the largest marginal sea in the western Pacific, the SCS is highly important in regard to material transport and accumulation (Wu et al., 2018). The SCS has preserved 5.5% of the global total sediment mass since its formation (Wang and Li, 2009), although it occupies 0.9% of the global sea area. The sediment influx calculations and transport pathways can be well constrained because the SCS is a semiclosed marginal sea (Liu et al., 2016). The SCS has a significant response to global climate change due to its high deposition rate and provides an ideal window to study the regional response to global changes (Wang, 1999; Wang and Li, 2009). Based on abundant sediment cores drilled mainly by oil companies, previous studies have focused on the shelf basins of the SCS, such as the Pearl River Mouth Basin (Su et al., 1989; Shao et al., 2008; Clift et al., 2014), the Yinggehai Basin (Clift, 2006; Lei et al., 2015), the Indochina Peninsula continental margin (Liu et al., 2007a; Liu et al., 2007b), and the Dangerous Grounds (Hinz and Schlüter, 1985; Clift et al., 2008; Ding et al., 2013).

In recent years, the deep-sea sediments in the SWSB and the East Sub-basin of the South China Sea have been analysed with constraints from the International Ocean Discovery Program (IODP) Expedition 349 drilling and surface sediment sampling (Li et al., 2014; Wu et al., 2018). However, there are still many controversies about the source and transport mode of sediments in the SWSB. Some records of sediment cores in the southern SCS indicate that the sediments deposited during the interglacial period were primarily sourced from the Mekong River (Liu et al., 2004, 2005; Colin et al., 2010; Fu et al., 2011; Liu et al., 2017; Jiwarrungueangkul et al., 2019a), northern Borneo (Steinke et al., 2006), or a mixture of sediments from the Mekong River and northern Borneo, with minor contributions from surrounding islands like Luzon/Palawan and/or Malay Peninsula/Sumatra (Steinke et al., 2008; Huang et al., 2016; Wan et al., 2017; Jiwarrungueangkul et al., 2019b). Previous studies have investigated the provenance of the SWSB through the analysis of clay minerals and have indicated that the Mekong River is the major contributor of fine-grained sediments to the SWSB, with minor contributions from the Luzon and/or Palawan island and northern Borneo. These fine-grained sediments are carried to the deep-sea basin through surface currents (Huang et al., 2021). However, we do not know whether the SWSB contains coarse sediments. If so, how are these coarse sediments transported to the deep-sea basin?

In this paper, fourteen sediment cores collected during the Marine IV/HYIV20150816 survey cruise in the North Nansha Block and SWSB of the SCS are used to analyse the trends of major elements, magnetic susceptibility, grain size, mineralogy, and geochemistry with the aim of investigating the sediment sources, transport and influences of the deep-sea sediments in the SWSB of the SCS (Figure 1).

## 2 Geologic setting and ocean current circulation

The SCS is tectonically located at the junction of the Eurasian, Pacific, and Indo-Australian Plates. The area of SCS has undergone continental rifting, seafloor spreading, and post spreading subsidence and subduction (Cao et al., 2017; Yin et al., 2021). The SCS is structurally subdivided into three subbasins: The East, Southwest and Northwest Subbasins (Figure 1). The SWSB is the deepest part of the SCS, with a water depth of 3000–4500 m. It is a V-shaped triangular subbasin with an area of 115,000 km<sup>2</sup> opening to the northeast with a distinct approximately 600 km-long NE–SW trending spreading ridge (Figure 1). The SWSB is surrounded by several tectonic units: the East Subbasin, which is separated by the Zhongnan Fault Zone in the east, the Nansha Block in the south, and the Paracel Islands and the Macclesfield Bank (Zhongsha Islands), as well as the Vietnamese continental margin, in the west (Figure 1). Seamounts of different sizes have developed on the flat seafloor, and two remarkable linear basement highs with a NE-oriented central rift graben are clearly visible in the bathymetric map (Figure 1B). According to the U1433 and U1434 drilling data reported by the IODP349 voyage, the shallow sediments in the SWSB are mainly clay or claystone (Figure 1D), and the deposition rate is approximately 20 cm/ky (Figure 1C). The sedimentary thickness at the mid-ocean ridge is more than 800 m.

Surface currents in the SCS are complex and influenced by the Asian monsoon and the Kuroshio Current intrusion (Shaw and Chao, 1994; Bao et al., 2019). The dominant basin-scale circulations in the upper layer driven by the winter and summer monsoons are cyclonic and anticyclonic, respectively, and the major circulation in the SCS is controlled by the winter monsoon (Wyrski, 1961; Jiwarrungueangkul and Liu, 2021). According to the available current models, the SWSB has complex surface circulation, which is mainly affected by the SCS Southern Anticyclonic Gyre and the SE Vietnam Offshore Current in summer and the Southern Cyclonic Gyre in winter (Fang et al., 1998).

The deep SCS is completely isolated below approximately 2400 m and has no direct water exchange with the surrounding ocean (Qu et al., 2006). The Bashi Strait is the main deep channel connecting the South China Sea and the Pacific Ocean (Chang et al., 2010). An overflow is believed to exist in the Luzon Strait because the deep-water properties of the SCS are rather homogeneous and similar to those of the Pacific at depths greater than 2000 m (Qu, 2002). The colder and denser Pacific water flows through the Luzon Strait and sinks into the SCS due to a persistent baroclinic pressure gradient (Wyrski, 1961; Qu et al., 2006). After entering the SCS, the overflow turns northwestwards and joins a basin-scale cyclonic circulation in the deep SCS flowing westwards, southwards and eastwards along the northern, western and southern margins, respectively (Qu et al., 2006; Wang et al., 2011). The southwards current to the east of the Zhongsha Islands is strengthened by the topographic effects of the central SCS seamounts, while another branch flows southwestwards along the boundary, forming a weak cyclonic circulation in the deep SWSB (Wang et al., 2018).

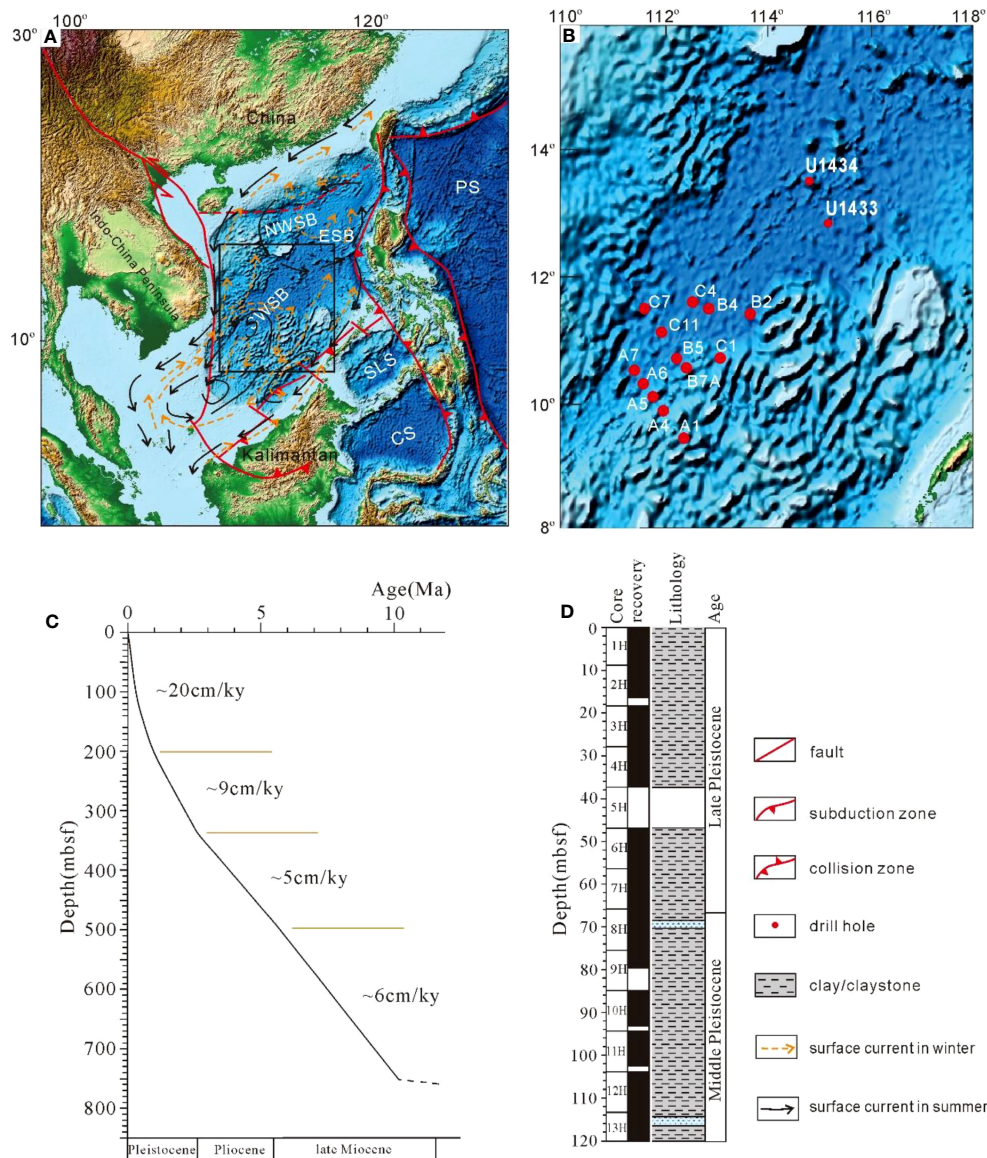


FIGURE 1

Tectonic-sedimentary characteristics of the study area. (A) Topographic map of the South China Sea. (B) The sampling sites (the red solid circles) in the SWSB and adjacent shelf in 2015. (C) The sedimentation rate in the SWSB. (D) The sedimentary histogram of the SWSB. c and d are modified from the IODP report (doi:10.14379/iodp.proc.349.105.2015). NWSB, northwestern sub-basin; ESB, eastern sub-basin; SWSB, southwestern sub-basin; SLS, Sulu Sea; CS, Celebes Sea; PS, Philippine Sea.

### 3 Materials and methods

Fourteen gravity cores used in this study were collected during the Marine IV/HYIV20150816 survey cruise in the SWSB and adjacent shelf in 2015. The locations and water depths of the sampling sites are shown in Figure 1 and Table 1. These sites cover the whole southwestern SWSB, which is conducive to studying regional deposition in the SWSB. The longest sedimentary core (C7) is 5 m long, and the shallow sedimentation rate of the SWSB is 20 cm/ky (Figure 1C) according to the IODP349 voyage report. Therefore, we estimate that the maximum age of our sedimentary core is approximately 25,000 years.

The major elements, magnetic susceptibility, and colours of the core columns were obtained by an XRF core scanner at intervals of

0.5–1 cm from the Guangzhou Marine Geological Survey. The column samples were cut in the middle and placed directly on the instrument for measurement. The results for major elements from the XRF core scanner are expressed as relative intensity and do not represent absolute content; rather, they represent relative percentage content. The higher the relative intensity is, the greater the corresponding element content. Al is often used to estimate the content of terrestrial detritus, but excess Al has recently been found in the SCS (Wei et al., 2003a). Ti in marine sediments is considered to be derived completely from terrigenous detritus, especially in the SCS (Wei et al., 2003b). The trend of the Ti content can reflect the variability in terrigenous input. The magnetic susceptibility trends generally indicate variations in the contents of diamagnetic and paramagnetic minerals in marine

TABLE 1 Sampling information for the sediment cores.

| Sample | Latitude (°N) | Longitude (°E) | Depth (m) | Length (m) | Note                 |
|--------|---------------|----------------|-----------|------------|----------------------|
| A1     | 9.4414        | 112.3785       | 1832      | 3.30       | Nansha Reef          |
| A4     | 9.8688        | 111.9781       | 2783      | 4.45       | Nansha Reef          |
| A5     | 10.1081       | 111.7839       | 3920      | 4.40       | COB                  |
| A6     | 10.316        | 111.5952       | 3853      | 2.65       | Sea basin            |
| A7     | 10.5153       | 111.4167       | 3759      | 3.00       | Sea basin            |
| B2     | 11.4309       | 113.6968       | 4335      | 3.80       | Sea basin            |
| B4     | 11.5015       | 112.8803       | 4245      | 3.80       | Sea basin            |
| B7A    | 10.5539       | 112.4501       | 4022      | 4.00       | COB                  |
| C1     | 10.7183       | 113.0789       | 3357      | 4.80       | Nansha Reef          |
| C4     | 11.5984       | 112.5551       | 4265      | 3.57       | Sea basin            |
| C7     | 11.4892       | 111.633        | 4050      | 5.00       | Western margin slope |
| C11    | 11.1427       | 111.932        | 4058      | 4.85       | Sea basin            |

sediments. The results for the colours were represented by the CIELab colour model. Because of the slight changes in the a and b values of the colour index, only the L value was selected.

The grain sizes of Cores A5 and C4 were analysed by a laser diffraction particle-size analyser (Beckman Coulter LS13320) at the School of Marine Science, Sun Yat-sen University, with an analytical range of 0.4–2000  $\mu\text{m}$  at intervals of 2  $\mu\text{m}$ .

Sediments at different depths (Sites A4, A5, B5, B6 and C4) were selected for mineral composition analysis via X-ray powder diffraction (XRD) at the Testing Centre of Sun Yat-sen University. The diffraction angle was in a range of 3–70°, and the scanning rate was 5°/min. Jade software and the PDF2 database were used to identify the mineral composition.

Parts of the sediments from the A5, B6 and C4 sites were dried and ground to determine the whole-rock trace element contents and Sr–Nd isotope ratios. The organic carbon and carbonate in the sediments were removed by  $\text{H}_2\text{O}_2$  and acetic acid, and then the samples were digested with concentrated  $\text{HNO}_3$  and HF. The sample solution was eluted by a Bio-Rad AG50W-X8 cation exchange column, the matrix elements and Rb were removed by 2.0 mol/L HCl, the Sr components were leached with 2.5 mol/L HCl, and finally, the total rare earth components were leached with 6.0 mol/L HCl. The Sr component of the previous step was further purified by SR special resin. For the purification of Nd, Sm and Nd were separated by an LN exchange column. The isotope ratios of Sr and Nd were measured by a Nu Plasma II MC–ICP–MS at Nanjing FocuMS Technology Co., Ltd. During the test,  $^{86}\text{Sr}/^{88}\text{Sr}=0.1194$  and  $^{146}\text{Nd}/^{144}\text{Nd}=0.7219$  were used as internal calibration instruments for mass fractionation, and NIST SRM 987 and Nd isotope JNDI-1 were used as external calibration instruments for drift.

The trace elements were tested and analysed by Nanjing FocuMS Technology Co., Ltd. Samples were processed by acid digestion: 40 mg of whole-rock powder was weighed and placed into the PTFE sample solution, 0.5 mL of concentrated nitric acid and 1.0 mL of concentrated hydrofluoric acid were added, and the sample solution was sealed by a steel sleeve and heated in a 195°C oven for 3 days to ensure complete

digestion. Sampling pellets containing digestion solution were steamed to wet salt on an electric heating plate, 6 ml of 20 wt% nitric acid was added, and the sample pellets were sealed again and placed in an oven at 195°C overnight. Finally, approximately 6 ml of the digestion solution was transferred to a centrifuge tube and weighed on a balance. The appropriate dilution (relative to the solid weight, a dilution factor of 2000 times) was used for atomization into an Agilent 7700X quad rod ICP–MS instrument for the determination of trace elements. Basalt BIR-1, BHVO-2, BCR-2, andesite AGV-2, rhyolite RGM-2, and granodiorite GSP-2 were used as the blind samples for quality control.

## 4 Results

### 4.1 Core description

Core scanning analysis revealed that the sediments in the cores are predominantly grey, grey–green and brown, with dark and red colours at certain depths. The sediments in the continental slope area (Sites A1, A4, C1, C7 and C11) are homogeneous and are dominated by fine-grained deep-sea clays. The shallow sediments at Sites A1 and A4 also contain a thicker layer of light-coloured calcareous ooze. The sediments in the sea basin (Sites A5, A6, A7, B2, B4, B7A and C4) varies greatly, with a large amount of silt and sandy sediment in addition to clay; dark sediment sections are well developed, and a thick layer of sand with foraminifera appears in some sections (Site A7).

### 4.2 Major elements and physical properties

The changes in major elements in the deep-sea basin are obviously much greater than those in the North Nansha Block. The trend lines of major elements show that K, Si, Al, Ti and Fe are relatively consistent, while Ca is negatively correlated with other elements (Figure 2). The major elements, magnetic susceptibility

and L values have relatively positive correlations. Carbonates in marine sediments have a significant dilution effect on terrestrial elements, leading to changes in Ca that are mostly contrary to or weakly correlated with Ti and other elements, as well as magnetic susceptibility and L values. Peaks in the trend lines of major elements often correspond to abrupt changes of the minerals in sediments or dark minerals. This characteristic can also be observed from the magnetic susceptibility and colour curves.

The trend lines show that the intensity of Ca is high in the surface layer, but the magnetic susceptibility is low, and the L values are stable throughout the whole core on Nansha Reef (Figure 2).

However, the major elements have strong variations, with more than one peak in the 10 cores from the deep-sea basin. The variations at Sites A5, A6 and A7 are close to those in the Sunda Shelf and Guangya Slope at the tip of the SWSB. The trend lines of A5 show that the relative contents of major elements are greater below 175 cm depth, with two distinct peaks in susceptibility at depths of approximately 175 cm and 335 cm where there are dark sediment sections in the cores (Figure 2). Sites A6 and A7 have similar variations with higher element contents at two depths: 50 cm in both shallow layers, 150–200 cm in A6 and 100–200 cm in A7. The variation in susceptibility also indicates peaks at approximately 117–145 cm and 265 cm in A6 and at approximately 124–129 cm and 209–214 cm in A7, also representing dark sediment sections in the cores (Figure 2).

The relative Ca contents at most sites in the deep-sea basin are low and steady, which is contrary to the high Ca contents in the North Nansha Block, especially in the shallow layer. In addition, we measured the highest Ca content in the deep layer of Site B2, which shows Ca peaks in the 2.5–2.7 m and 3.7 m layers in the trend line and light-coloured sand containing foraminifera in the sediment core (Figure 2). Dark sediment sections are found at depths of 64–70 cm, 235 cm and 269–274 cm with relatively high susceptibility and L values (Figure 2).

There are three changes in the contents of major elements at Site B7A. The dark sediment sections are found at depths of 105, 285–288 and 320 cm (Figure 2).

The trends of the major elements at Site B4 are stable, which shows that the relative content decreased gradually from the past to the present, but these trends are sharp at Site C4, with several peaks (Figure 2). Sites B4 and C4 show many dark layers with changes in susceptibility and L values: a shallow black layer enriched in organic matter at 37–53 cm and dark sediment sections at depths of approximately 140, 154–159, 168–172 and 213–216 cm at Site B4; and dark sediment sections at 140, 144–160 and 170–186 cm and a deep black layer containing organic matter at 230–239 cm at Site C4.

The elemental changes at Sites C1, C7 and C11 are also strong compared with those at the above sites, and some sporadic dark sediment sections are found in the cores: a dark sediment section at 156 cm and some dark sediment sections at Site C7 and at a depth of 385 cm with a susceptibility peak at Site C11 (Figure 2).

### 4.3 Characteristics of grain size

The grain-size distribution curves at Sites A5 and C4 show that there are multiple layers of coarse-grained sediments (Figure 3). In the normal deep-sea sediments at Site A5, the median particle size generally varies between 4 and 10  $\mu\text{m}$ , the average proportions of clay (< 4  $\mu\text{m}$ ) and silt (4–63  $\mu\text{m}$ ) are approximately 40% and 60%, respectively, and the sediment content of the sand (> 63  $\mu\text{m}$ ) is almost zero. Coarse-grained sediments are located at 160–180 cm, 280–300 cm and 320–340 cm, with median grain sizes of 125  $\mu\text{m}$ , 27  $\mu\text{m}$  and 46  $\mu\text{m}$ , respectively. All coarse particles are located in dark sediment sections. The coarse-grained layer is mainly composed of sandy sediments with a content of 30–75%. The silt content is 10–50%, especially in the coarse grain layer at 160–180 cm, where the silt content decreases most obviously. The clay content in the

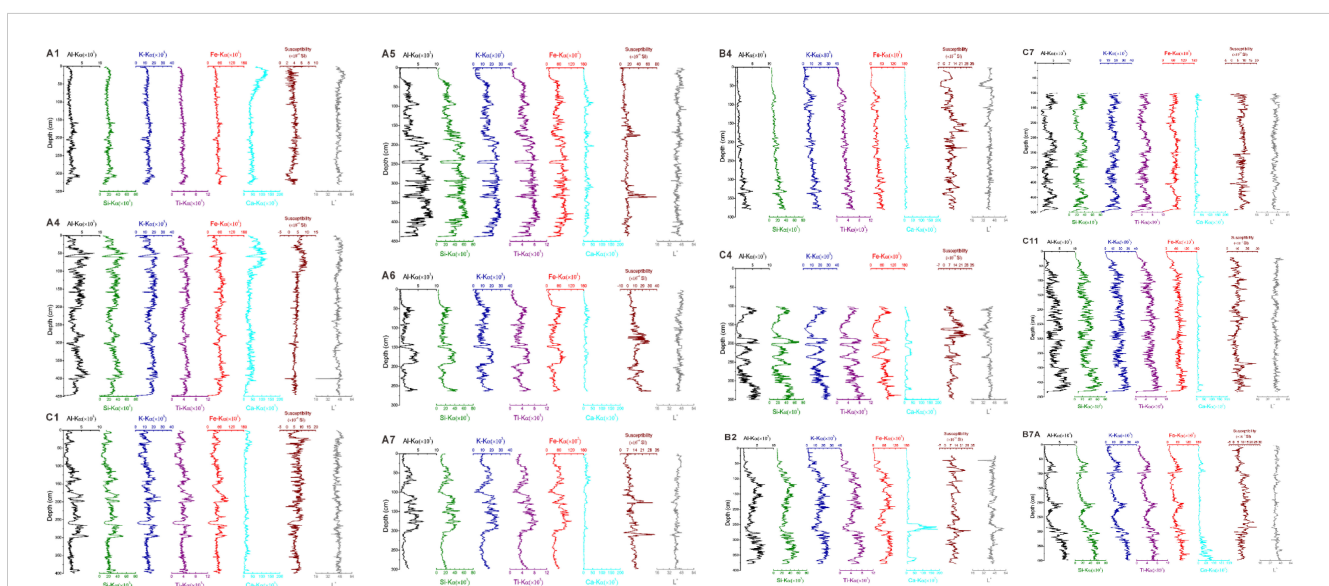
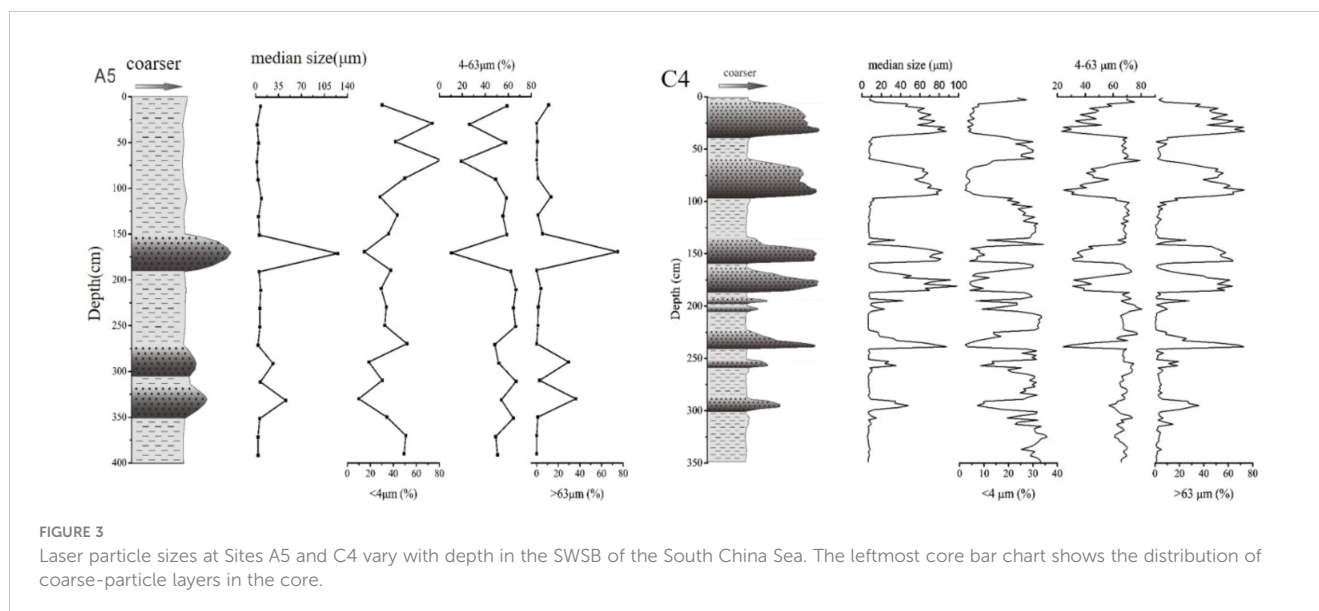


FIGURE 2 Trends of major elements, susceptibility and L values in core sediments from the sites.



coarse-grained layer is significantly reduced from an average of 40% in the deep-sea ooze sediment to 10–15% in the coarse-grained layer.

The grain-size curves at Sites C4 show several high peaks (Figure 3). The core bar chart shows the distribution of coarse-particle layers in the core. In normal deep-sea sediments, the median particle-size range is approximately 6–12  $\mu\text{m}$ , the average contents of clay (<4  $\mu\text{m}$ ) and silt (4–63  $\mu\text{m}$ ) are approximately 30% and 70%, respectively, and the content of sand (>63  $\mu\text{m}$ ) is almost zero (Figure 3). At the bottom of the coarse layer, the median grain-size range is approximately 80–100  $\mu\text{m}$ , and it becomes fine upwards, having a typical normal grading. The range of sand content in the coarse layer is 20–70%, which has the most obvious influence on the median particle size and is obviously related to the coarse-particle layers. The clay and silt grain sizes decrease significantly in the coarse layer. The coarse grains corresponding to the four small peaks are dominated by silt, with an average content of 60–80%.

#### 4.4 Mineralogical characteristics

The XRD results (Figure 4) show that the sediments at Sites A4, A5, B5, B6 and C4 are mainly composed of quartz, feldspar, clay minerals, muscovite, biotite and hornblende, and some sediments contain calcite and other calcareous carbonate minerals. Quartz is dominant in the sediments, and the content of quartz is higher compared to that in other sea basin. Carbonate minerals such as calcite are mainly distributed in the sediments at Site A4. The XRD characteristic peaks of sediments at two depths at Site A4 in the Nansha Block are very similar. The quartz characteristic peaks in the middle (160–180 cm) and deep (280–300 cm) sediments at Site A5 are significantly greater than those in the shallow (0–20 cm) sediments, and there are potassium feldspar peaks with greater intensity in the middle. High contents of quartz and plagioclase and

small amounts of amphibole and biotite are present at Site B6. At Site C4, plagioclase peaks are more intense in the shallow (0–20 cm) and middle (80–100 cm) layers, and potassium feldspar peaks are most significant in the shallow layer.

#### 4.5 Trace elements

In general, the trace element results show that the average trace element contents of the core sediments from Sites A5, B6 and C4 are relatively lower than the average values of the upper continental crust (UCC) in Sc, Cr, Co, Ni, Cu, Y, Nb, Ba and Ta. However, the contents of Rb, Zr, Cs and HF are relatively high (Figure 5). The contents of Co, Ni, Cu, Y and Ba in the core sediments are significantly lower than those in the Western Pacific Brown Clay. Compared with those of the post-Archean Australian Shale (PAAS), the contents of other trace elements are low or similar except for the high Nb content. In addition, there are some differences in the trace element concentrations in the sediments from the different sites. Compared with B6, Sites A5 and C4 have higher contents of Zr and HF, while B6 have a higher Ba content.

Table 2 shows that the contents of total rare earth elements (REEs) in the sediments are slightly lower than those in the UCC, ranging from  $106.52\text{--}136.73 \times 10^{-6}$ . The total light rare earth elements ( $\Sigma\text{LREEs}$ ) and heavy rare earth elements ( $\Sigma\text{HREEs}$ ) are in the ranges of  $93\text{--}124 \times 10^{-6}$  and  $10.6\text{--}13.6 \times 10^{-6}$ , respectively. The  $\Sigma\text{LREE}/\Sigma\text{HREE}$  ratio ranges from 8.41 to 10.33, indicating enrichment of LREEs. After standardization to the REE contents of chondrites and the North American Shale Composite (NASC), the REE content distribution diagram of the core sediments at each site was obtained (Figure 6). The normalized REE distribution curves of the sediments by chondrite and NASC at the three sites are similar. Compared with chondrites, LREEs are relatively enriched, while HREEs are relatively depleted. The values of  $\delta\text{Eu}$  ( $\delta\text{Eu} = \text{Eu}_n / (\text{SM}_n * \text{Gd}_n)^{1/2}$ ) are all less than 1, indicating depletion

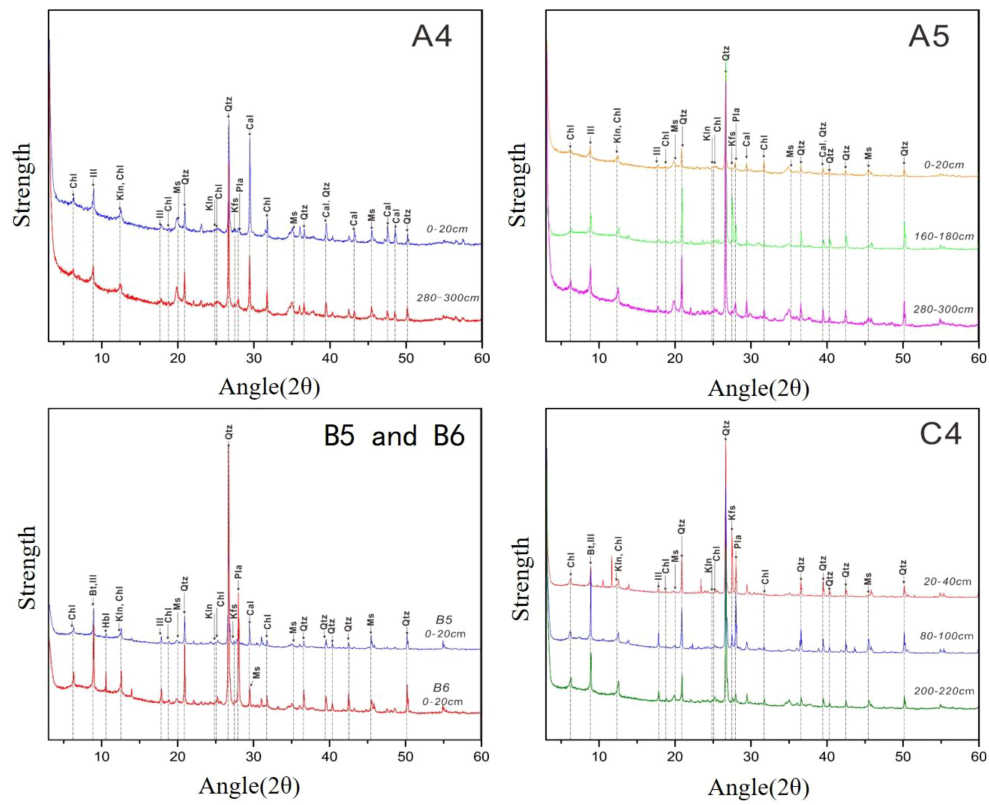


FIGURE 4 Whole-rock diffraction pattern of core sediments at Sites A4, A5, B7A, B6 and C4. Chl, chlorite; Bt, biotite; Cal, calcite; Hbl, hornblende; Ill, illite; Kfs, K-feldspar; Kln, kaolinite; Ms, muscovite; Pla, plagioclase; Qtz, quartz.

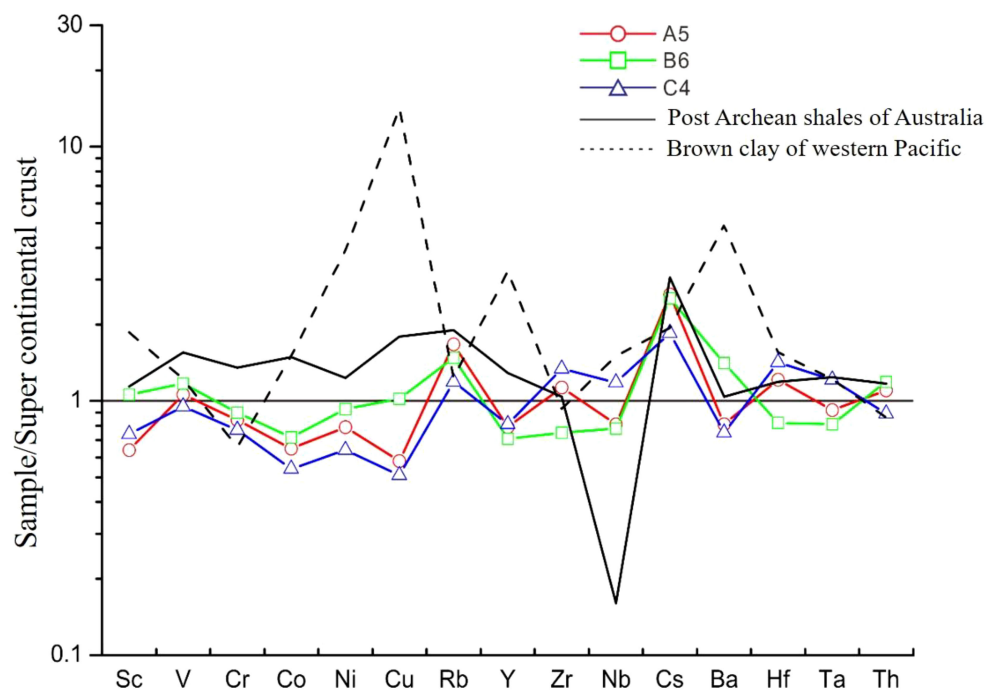


FIGURE 5 Spider diagram of trace elements in core sediments of the Southwest Sub-basin in the South China Sea.

TABLE 2 Contents of trace and rare earth elements ( $\times 10^{-6}$ ) and some characteristic parameters for core sediments from the Southwest Sub-basin.

|           | A5<br>(40-60) | A5<br>(180-200) | A5<br>(320-340) | B6<br>(20-40) | B6<br>(80-100) | C4<br>(20-40) | C4<br>(180-200) | C4<br>(320-340) |
|-----------|---------------|-----------------|-----------------|---------------|----------------|---------------|-----------------|-----------------|
| <b>Li</b> | 72.0          | 57.8            | 54.8            | 85.2          | 79.6           | 35.1          | 51.8            | 82.2            |
| <b>Be</b> | 2.48          | 2.37            | 2.35            | 2.40          | 2.39           | 1.70          | 2.03            | 2.46            |
| <b>B</b>  | 115           | 137             | 110             | 92.5          | 105            | 77.9          | 93.6            | 126             |
| <b>Sc</b> | 9.45          | 8.65            | 8.91            | 16.5          | 13.1           | 8.63          | 9.80            | 12.5            |
| <b>Ti</b> | 2280          | 2040            | 2122            | 2513          | 2248           | 1899          | 4165            | 4301            |
| <b>V</b>  | 108           | 104             | 95.0            | 113           | 113            | 58.4          | 86.8            | 130             |
| <b>Cr</b> | 80.0          | 75.7            | 77.4            | 85.2          | 79.9           | 60.1          | 68.2            | 85.5            |
| <b>Mn</b> | 315           | 245             | 210             | 325           | 232            | 203           | 269             | 393             |
| <b>Co</b> | 12.9          | 10.9            | 9.65            | 13.1          | 11.8           | 6.72          | 8.45            | 12.6            |
| <b>Ni</b> | 45.2          | 34.5            | 31.4            | 45.8          | 41.7           | 19.9          | 26.9            | 43.3            |
| <b>Cu</b> | 21.3          | 15.0            | 12.5            | 32.3          | 25.1           | 7.81          | 12.0            | 23.2            |
| <b>Zn</b> | 110           | 90.7            | 82.2            | 114           | 96.9           | 52.2          | 70.0            | 98.1            |
| <b>Ga</b> | 18.9          | 18.6            | 18.2            | 21.9          | 20.0           | 13.2          | 16.0            | 21.1            |
| <b>As</b> | 5.85          | 19.7            | 10.4            | 5.96          | 7.88           | 4.83          | 7.18            | 9.07            |
| <b>Se</b> | 1.04          | 0.94            | 0.84            | 1.09          | 0.97           | 0.75          | 0.73            | 0.89            |
| <b>Rb</b> | 142           | 146             | 132             | 142           | 107            | 87.4          | 94.5            | 118             |
| <b>Sr</b> | 75.4          | 82.7            | 83.6            | 80.0          | 82.3           | 102           | 87.7            | 70.6            |
| <b>Y</b>  | 15.3          | 16.3            | 18.1            | 15.3          | 14.8           | 20.0          | 16.1            | 14.9            |
| <b>Zr</b> | 157           | 188             | 312             | 130           | 160            | 359           | 261             | 157             |
| <b>Nb</b> | 10.5          | 9.12            | 9.49            | 10.0          | 8.65           | 9.02          | 16.7            | 16.7            |
| <b>Mo</b> | 0.16          | 0.28            | 0.17            | 0.19          | 0.15           | 0.09          | 0.31            | 0.29            |
| <b>Sn</b> | 3.09          | 2.70            | 2.67            | 3.02          | 2.76           | 1.72          | 3.16            | 4.12            |
| <b>Cs</b> | 12.6          | 13.6            | 12.3            | 12.7          | 12.1           | 5.43          | 8.60            | 13.2            |
| <b>Ba</b> | 681           | 435             | 401             | 1035          | 725            | 444           | 426             | 528             |
| <b>La</b> | 29.7          | 31.9            | 33.5            | 28.0          | 23.8           | 29.9          | 25.8            | 25.3            |
| <b>Ce</b> | 48.4          | 52.1            | 55.1            | 46.7          | 42.1           | 51.5          | 44.0            | 42.3            |
| <b>Pr</b> | 6.05          | 6.46            | 6.95            | 5.70          | 5.22           | 6.30          | 5.54            | 5.40            |
| <b>Nd</b> | 20.6          | 21.9            | 23.6            | 19.4          | 17.9           | 21.7          | 19.0            | 18.4            |
| <b>Sm</b> | 3.64          | 3.80            | 4.14            | 3.39          | 3.27           | 3.94          | 3.48            | 3.37            |
| <b>Eu</b> | 0.68          | 0.72            | 0.76            | 0.65          | 0.64           | 0.74          | 0.64            | 0.65            |
| <b>Gd</b> | 2.96          | 3.10            | 3.42            | 2.77          | 2.73           | 3.50          | 2.96            | 2.78            |
| <b>Tb</b> | 0.48          | 0.50            | 0.55            | 0.46          | 0.47           | 0.58          | 0.48            | 0.46            |
| <b>Dy</b> | 2.77          | 2.85            | 3.20            | 2.67          | 2.81           | 3.55          | 2.86            | 2.76            |
| <b>Ho</b> | 0.58          | 0.61            | 0.67            | 0.55          | 0.59           | 0.74          | 0.61            | 0.59            |
| <b>Er</b> | 1.72          | 1.78            | 2.02            | 1.68          | 1.79           | 2.18          | 1.81            | 1.80            |
| <b>Tm</b> | 0.29          | 0.31            | 0.34            | 0.29          | 0.32           | 0.37          | 0.32            | 0.32            |
| <b>Yb</b> | 1.86          | 1.87            | 2.15            | 1.88          | 2.01           | 2.28          | 2.06            | 2.04            |
| <b>Lu</b> | 0.28          | 0.30            | 0.35            | 0.30          | 0.33           | 0.37          | 0.33            | 0.33            |

(Continued)

TABLE 2 Continued

|                      | A5<br>(40-60) | A5<br>(180-200) | A5<br>(320-340) | B6<br>(20-40) | B6<br>(80-100) | C4<br>(20-40) | C4<br>(180-200) | C4<br>(320-340) |
|----------------------|---------------|-----------------|-----------------|---------------|----------------|---------------|-----------------|-----------------|
| Hf                   | 4.75          | 5.64            | 8.89            | 3.92          | 4.78           | 10.2          | 7.64            | 4.74            |
| Ta                   | 0.90          | 0.78            | 0.80            | 0.80          | 0.67           | 0.66          | 1.28            | 1.31            |
| W                    | 1.44          | 1.27            | 1.17            | 1.42          | 1.06           | 0.89          | 1.66            | 1.81            |
| Tl                   | 1.05          | 0.92            | 0.88            | 1.03          | 1.04           | 0.55          | 0.77            | 1.03            |
| Pb                   | 13.4          | 12.5            | 11.8            | 13.0          | 13.1           | 9.76          | 9.94            | 12.6            |
| Bi                   | 0.20          | 0.16            | 0.16            | 0.20          | 0.21           | 0.08          | 0.09            | 0.20            |
| Th                   | 12.6          | 10.7            | 11.3            | 14.2          | 10.8           | 9.74          | 8.64            | 9.57            |
| U                    | 2.40          | 2.39            | 2.57            | 2.31          | 2.29           | 2.16          | 1.99            | 2.10            |
| ΣREE                 | 119.91        | 128.15          | 136.73          | 114.40        | 103.99         | 127.58        | 109.87          | 106.52          |
| ΣLREE                | 109           | 117             | 124             | 104           | 93             | 114           | 98              | 95              |
| ΣHREE                | 10.9          | 11.3            | 12.7            | 10.6          | 11.0           | 13.6          | 11.4            | 11.1            |
| δEu                  | 0.58          | 0.59            | 0.57            | 0.60          | 0.60           | 0.56          | 0.57            | 0.59            |
| δCe                  | 0.87          | 0.87            | 0.87            | 0.89          | 0.91           | 0.90          | 0.88            | 0.87            |
| L/H                  | 9.98          | 10.33           | 9.77            | 9.79          | 8.42           | 8.41          | 8.62            | 8.61            |
| (La/Sm) <sub>n</sub> | 4.34          | 4.47            | 4.30            | 4.40          | 3.88           | 4.03          | 3.95            | 4.00            |
| (Gd/Yb) <sub>n</sub> | 1.28          | 1.34            | 1.28            | 1.19          | 1.10           | 1.24          | 1.16            | 1.10            |
| La/Y                 | 1.94          | 1.95            | 1.85            | 1.84          | 1.61           | 1.49          | 1.60            | 1.69            |
| Nb/Ta                | 11.66         | 11.65           | 11.87           | 12.59         | 12.88          | 13.63         | 13.00           | 12.76           |
| Zr/Hf                | 32.94         | 33.28           | 35.07           | 33.14         | 33.58          | 35.11         | 34.08           | 33.09           |
| Th/Sc                | 1.33          | 1.24            | 1.27            | 0.86          | 0.82           | 1.13          | 0.88            | 0.77            |
| La/Sc                | 3.14          | 3.69            | 3.76            | 1.70          | 1.81           | 3.46          | 2.64            | 2.03            |
| Th/Cr                | 0.16          | 0.14            | 0.15            | 0.17          | 0.13           | 0.16          | 0.13            | 0.11            |
| La/Co                | 2.30          | 2.92            | 3.47            | 2.13          | 2.02           | 4.44          | 3.06            | 2.00            |
| Th/Co                | 0.98          | 0.98            | 1.17            | 1.08          | 0.91           | 1.45          | 1.02            | 0.76            |
| La/Nb                | 2.82          | 3.50            | 3.53            | 2.80          | 2.75           | 3.31          | 1.55            | 1.51            |
| Rb/Sr                | 1.88          | 1.76            | 1.58            | 1.78          | 1.30           | 0.86          | 1.08            | 1.67            |

L/H=ΣLREE/ΣHREE, where *n* is the standardization of chondrite, and chondrite data are from (Boynton, 1984).

of Eu. The value of δCe ( $\delta\text{Ce} = \text{Ce}_n / (\text{La}_n * \text{Pr}_n)^{1/2}$ ) is close to 1, and an anomaly pattern is not obvious. The REE distribution patterns of the three sites are consistent with those of the NASC, and the REE contents of the three sites are slightly lower than those of the NASC. The standardization curve of the NASC is flat, the enrichment and depletion of LREEs and HREEs are not obvious, and both Eu and Ce show weak negative anomalies.

## 4.6 Sr and Nd isotopes

The Sr–Nd isotope ratios of core sediments show that the ratios of  $^{87}\text{Sr}/^{86}\text{Sr}$  and  $^{143}\text{Nd}/^{144}\text{Nd}$  of sediments at Sites A5, B6 and C4 range from 0.718459–0.724064 and 0.512010–0.512058, respectively. The values of  $\epsilon_{\text{Nd}}$  range from -12.3 to -11.3 (Table 3).

## 5 Discussion

### 5.1 Sediment source

Previous studies have shown that the main provenances of the southern South China Sea are the Sunda Shelf, Borneo and their associated rivers (Tong, 2007; Liu et al., 2007a; Steinke et al., 2008; Huang et al., 2016). The Mekong River transports 160 Mt of sediment to the SCS per year (Milliman and Syvitski, 1992). The Baram and Rajang Rivers in northern Borneo transport 12 Mt (Hiscott, 2001) and 30 Mt (Staub et al., 2000) per year to the SCS basin, respectively. However, sediment flux data from the Malaysian and Indonesian islands as well as Sumatra are lacking. The evidence which terrigenous material from these rivers or continental margins reach the deep-sea basin is still sparse.

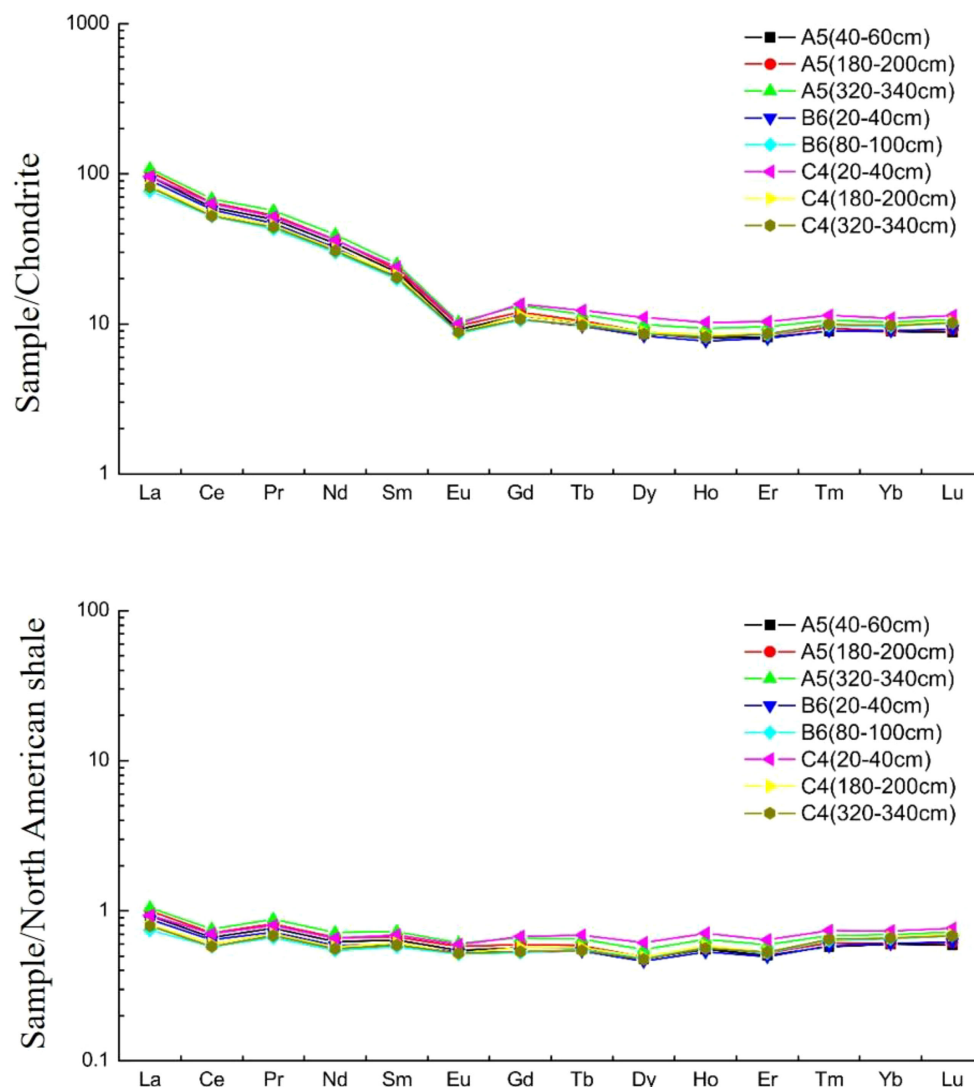


FIGURE 6  
REE standardized model of core sediments at Sites A5, B6 and C4. The NASC data are from Haskin and Haskin (1984).

Grain-size analysis (Figure 3) revealed that there are multiple layers of coarse-grained sediments in the sediments of the deep-sea basin, and the XRD results (Figure 4) revealed that the sediments contain mainly quartz with feldspar and clay minerals, in addition to dark minerals such as biotite, muscovite and hornblende. These results and previous research (Chen et al., 2004) indicate that there are multistage turbidite deposits in the SWSB of the SCS. The elemental fluctuations (Figure 2) in the deep-sea basin are much stronger than those in the northern Nansha Block (Sites A1, A4 and C1), the occurrence of multiple peaks in the contents of major elements reflects changes in terrestrial inputs, and the turbidites widely distributed in the deep-sea basin suggest instability of the sedimentary environment.

Sites A1, A4, B2 and C1, located in the northern Nansha Block, have similar core characteristics and elemental change curves (Figure 2), and the shallow surface sediments have relatively high contents of Ca, which is consistent with the rich biocarbonate deposits in the Nansha Block. The most obvious feature of Sites B2

is the presence of sand with foraminifera in the core located at 2.5–2.7 m and 3.7 m, and the elemental curve clearly shows two peaks in Ca (Figure 2). Ca has a low susceptibility and terrestrial elements show the dilution effect of Ca. The carbonate compensation depth (CCD) in the southern South China Sea is approximately 4000 m (Zhang et al., 2010). The water at B2 is deeper than 4300 m, and these two layers of sand with foraminifera are not *in situ* deposited?; therefore, we speculate that they represent biological turbidity current sediments transported from the adjacent Nansha Block. Caused by sedimentary events, this nonoriginal foraminiferal sand was rapidly transported to Sites B2 by gravity flow.

Sites A5, A6, A7 and B7A have similar core scanning characteristics and strong elemental variations with high relative contents of terrestrial elements (Figure 2). Their potential provenances include the Sunda Shelf, Nansha Block and associated rivers. In general, coarse-grained sediments have difficulty reaching deep-sea basins. Based on the development of multilayer turbidite deposits in the SWSB, we speculate that coarser

TABLE 3 Nd and Sr isotopes of partial core sediments in the Southwest Sub-basin.

| sample | depth(cm) | $^{87}\text{Sr}/^{86}\text{Sr}$ ( $2\sigma$ ) | $^{143}\text{Nd}/^{144}\text{Nd}$ ( $2\sigma$ ) | $\epsilon_{\text{Nd}}$ |
|--------|-----------|---|---|------------------------|
| A5-1   | 40-60     | 0.724064 ± 9                                  | 0.512036 ± 5                                    | -11.7                  |
| A5-2   | 180-200   | 0.723346 ± 8                                  | 0.512054 ± 4                                    | -11.4                  |
| A5-3   | 320-340   | 0.722940 ± 12                                 | 0.512051 ± 5                                    | -11.5                  |
| B6-1   | 20-40     | 0.722452 ± 9                                  | 0.512057 ± 5                                    | -11.3                  |
| B6-2   | 80-100    | 0.722254 ± 9                                  | 0.512058 ± 4                                    | -11.3                  |
| C4-1   | 20-40     | 0.718459 ± 7                                  | 0.512010 ± 3                                    | -12.3                  |
| C4-2   | 180-200   | 0.720743 ± 8                                  | 0.512037 ± 6                                    | -11.7                  |
| C4-3   | 320-340   | 0.723955 ± 12                                 | 0.512055 ± 5                                    | -11.4                  |

sediments were first deposited near the continental margin and continental shelf, with changes in sea level and the impacts of abrupt events (Chen et al., 2004, 2007). These relatively ancient sediments migrated to the deep sea by turbidity currents.

For the trace elements, the average values of La/Sc, Th/Sc, Th/Cr and Th/Co in the cores from the three sites in the SWSB are 1.75-3.53, 0.84-1.28, 0.13-0.15 and 1.00-1.08, respectively (Table 4), which are close to the UCC values. These sediments of the three sites are mainly from the surrounding continents. The contents of La-Th-Sc elements at the three sites are similar (Figure 7) and are

close to those of the western and southern margins of the SCS, suggesting their possible sources. The  $\delta\text{Eu-Th/Sc}$  contents diagram show that the core sediments of the three sites are far from provenances like andesite, TTG (trondhjemite, tonalite, and granodiorite) and basaltic source areas and close to the UCC (Figure 8). In addition, the Hf-La/Th discrimination diagram (Figure 9) shows that most of the sediments are close to the felsic source area (Cai et al., 2010). The distribution patterns of REE contents at Sites A5, B6 and C4 are similar to those of the Pearl River, Red River and Mekong River (Liu et al., 2007a, 2016)

TABLE 4 Average contents of trace and rare earth elements ( $\times 10^{-6}$ ) and some characteristic parameters for core sediments from the Southwest Sub-basin.

|                     | A5     | B6     | C4     | UCC   | PAAS  | Western Pacific Brown Clay |
|---------------------|--------|--------|--------|-------|-------|----------------------------|
| Sc                  | 9.00   | 14.83  | 10.30  | 14    | 16    | 26                         |
| V                   | 102.49 | 113.19 | 91.75  | 97    | 150   | 118                        |
| Cr                  | 77.70  | 82.53  | 71.26  | 92    | 124.5 | 61                         |
| Co                  | 11.16  | 12.47  | 9.26   | 17.3  | 25.7  | 26                         |
| Ni                  | 37.02  | 43.73  | 30.04  | 47    | 58    | 184                        |
| Cu                  | 16.29  | 28.68  | 14.32  | 28    | 50    | 396                        |
| Rb                  | 139.91 | 124.59 | 99.84  | 84    | 160   | 103                        |
| Y                   | 16.59  | 15.01  | 17.03  | 21    | 27    | 68                         |
| Zr                  | 218.67 | 145.24 | 258.66 | 193   | 200   | 180                        |
| Nb                  | 9.70   | 9.33   | 14.14  | 12    | 1.9   | 18                         |
| Cs                  | 12.84  | 12.41  | 9.08   | 4.9   | 15    | 9.5                        |
| Ba                  | 505.70 | 880.22 | 465.67 | 624   | 650   | 3060                       |
| Hf                  | 6.43   | 4.35   | 7.53   | 5.3   | 6.3   | 8.2                        |
| Ta                  | 0.83   | 0.73   | 1.08   | 0.9   | 1.12  | 1.1                        |
| Th                  | 11.53  | 12.46  | 9.32   | 10.5  | 12.3  | 9                          |
| $\Sigma\text{REE}$  | 128.26 | 109.20 | 114.66 | 148.1 | 173.0 | 142.1                      |
| $\Sigma\text{LREE}$ | 116.62 | 98.38  | 102.63 | 133.8 | 152.8 | 127.1                      |
| $\Sigma\text{HREE}$ | 11.64  | 10.82  | 12.02  | 14.34 | 20.11 | 14.98                      |

(Continued)

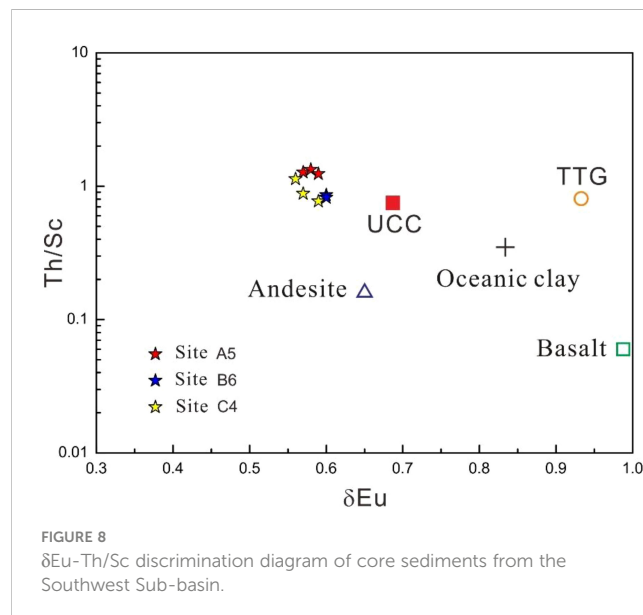
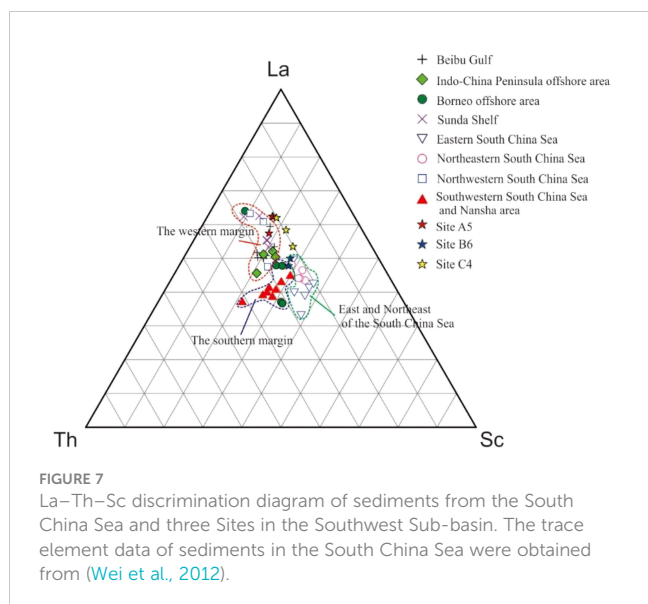
TABLE 4 Continued

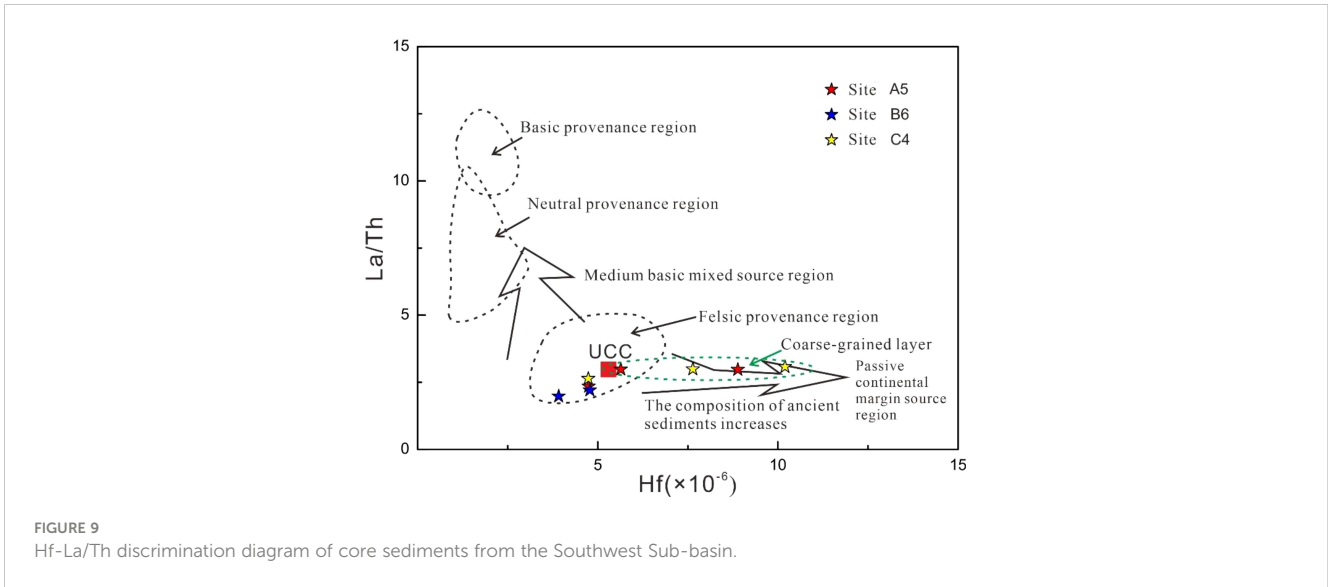
|                                    | A5    | B6    | C4    | UCC   | PAAS  | Western Pacific Brown Clay |
|------------------------------------|-------|-------|-------|-------|-------|----------------------------|
| $\delta\text{Eu}$                  | 0.58  | 0.60  | 0.57  | 0.69  | 0.68  | 0.83                       |
| $\delta\text{Ce}$                  | 0.87  | 0.90  | 0.89  | 0.97  | 1.05  | 0.93                       |
| L/H                                | 10.03 | 9.11  | 8.55  | 9.33  | 7.60  | 8.49                       |
| $(\text{La}/\text{Sm})_{\text{N}}$ | 4.37  | 4.14  | 3.99  | 4.15  | 3.53  | 2.46                       |
| $(\text{Gd}/\text{Yb})_{\text{N}}$ | 1.30  | 1.14  | 1.17  | 1.62  | 1.36  | 1.69                       |
| La/Y                               | 1.91  | 1.72  | 1.60  | 1.48  | 1.19  | 0.38                       |
| Nb/Ta                              | 11.73 | 12.73 | 13.13 | 13.33 | 1.70  | 16.36                      |
| Zr/Hf                              | 33.76 | 33.36 | 34.10 | 36.42 | 31.75 | 21.95                      |
| Th/Sc                              | 1.28  | 0.84  | 0.93  | 0.75  | 0.77  | 0.35                       |
| La/Sc                              | 3.53  | 1.75  | 2.71  | 2.21  | 2.00  | 1.00                       |
| Th/Cr                              | 0.15  | 0.15  | 0.13  | 0.11  | 0.10  | 0.15                       |
| La/Co                              | 2.90  | 2.08  | 3.17  | 1.79  | 1.25  | 1.00                       |
| Th/Co                              | 1.04  | 1.00  | 1.08  | 0.61  | 0.48  | 0.35                       |
| La/Nb                              | 3.28  | 2.78  | 2.12  | 2.58  | 16.84 | 1.45                       |

(Figure 6). Compared with chondrites, their LREEs are relatively enriched, HREEs are relatively depleted, and Eu shows a negative anomaly, but Ce has no obvious anomaly (Figure 6). Compared with those of the NASC, their distribution patterns are flat linear curves (Figure 6). All of their REE contents inherited the characteristics of terrigenous sediments. The whole-rock Sr–Nd isotope ratios show that the  $^{87}\text{Sr}/^{86}\text{Sr}$  and  $^{144}\text{Nd}/^{143}\text{Nd}$  ratios of the cores at different depths at the three sites in the deep-sea basin exhibit little variation (Figure 10). Previous geochemical investigations of sediment and river sediments revealed that the  $\epsilon_{\text{Nd}}$  values of seabed sediments are significantly correlated with

those of sediments from surrounding rivers (Figure 10). The distribution of  $\epsilon_{\text{Nd}}$  values in seafloor sediments is consistent with the potential sources of fluvial systems that feed terrigenous material into these areas (Liu et al., 2007a; Li et al., 2020). The results from the International Ocean Discovery Program (IODP) Expedition 349 Site U1433 (Bao et al., 2019) and other seabed surface samples (Wan et al., 2019) show that the organic carbon in the deep-sea basin of the SWSB is predominantly terrigenous.

Based on the above analysis, we confirm that the sediments in the SWSB were derived from terrigenous materials of multiple sources.



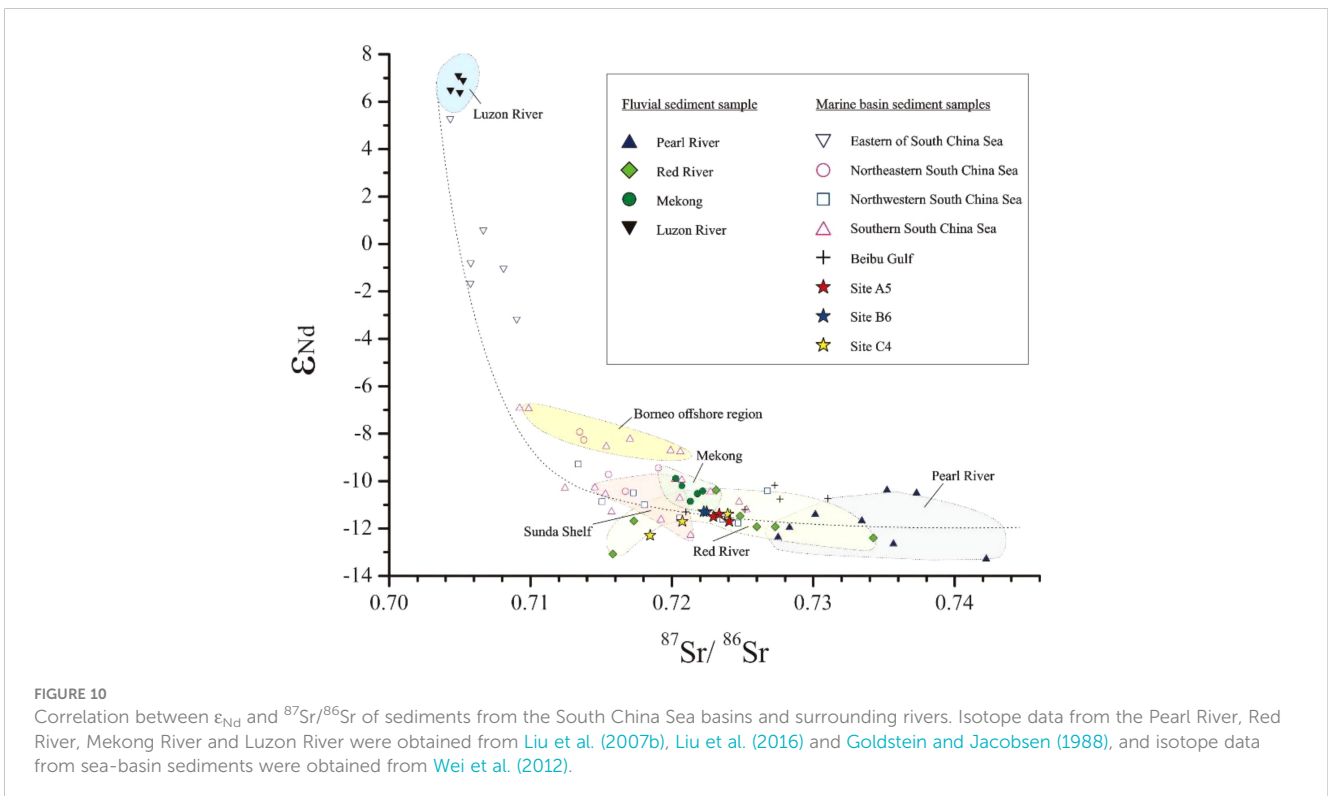


### 5.2 Sediment transport

Previous studies have been published on the composition, distribution and transport of clay minerals in the SCS (Liu et al., 2010a, b; Schroeder et al., 2015). Fine-grained sediments in the ocean containing clays are derived from rivers, and their spatial distribution is closely related to current patterns (Liu et al., 2016). By analysing the surface current systems of the SCS (Figure 11A), we find that sediments from the Red River can enter the deep-sea basin of the SWSB through surface currents in winter, and sediments from the Mekong River, Sunda Shelf and Nansha Block can enter the deep-sea basin of the

SWSB through surface currents in summer, which may also be the reason for the multiple provenances of the sediment in the SWSB. This paper mainly examines how coarse material enters the SWSB.

There are at least 6 distinct thick coarse-particle layers corresponding to 6 turbidity current deposits at Site C4 (Figure 3). These turbidite deposits contain many coarse materials (Chen et al., 2004; Zhao et al., 2011). Turbidites formed by rapid accumulation in deep-sea basins are not affected by surface circulation. Therefore, coarse-grained minerals can be transported to deep-ocean basins by gravity flows. Considering that turbidity currents cannot move over long distances, coarse materials in the deep-sea basin are interpreted to be mainly transported by



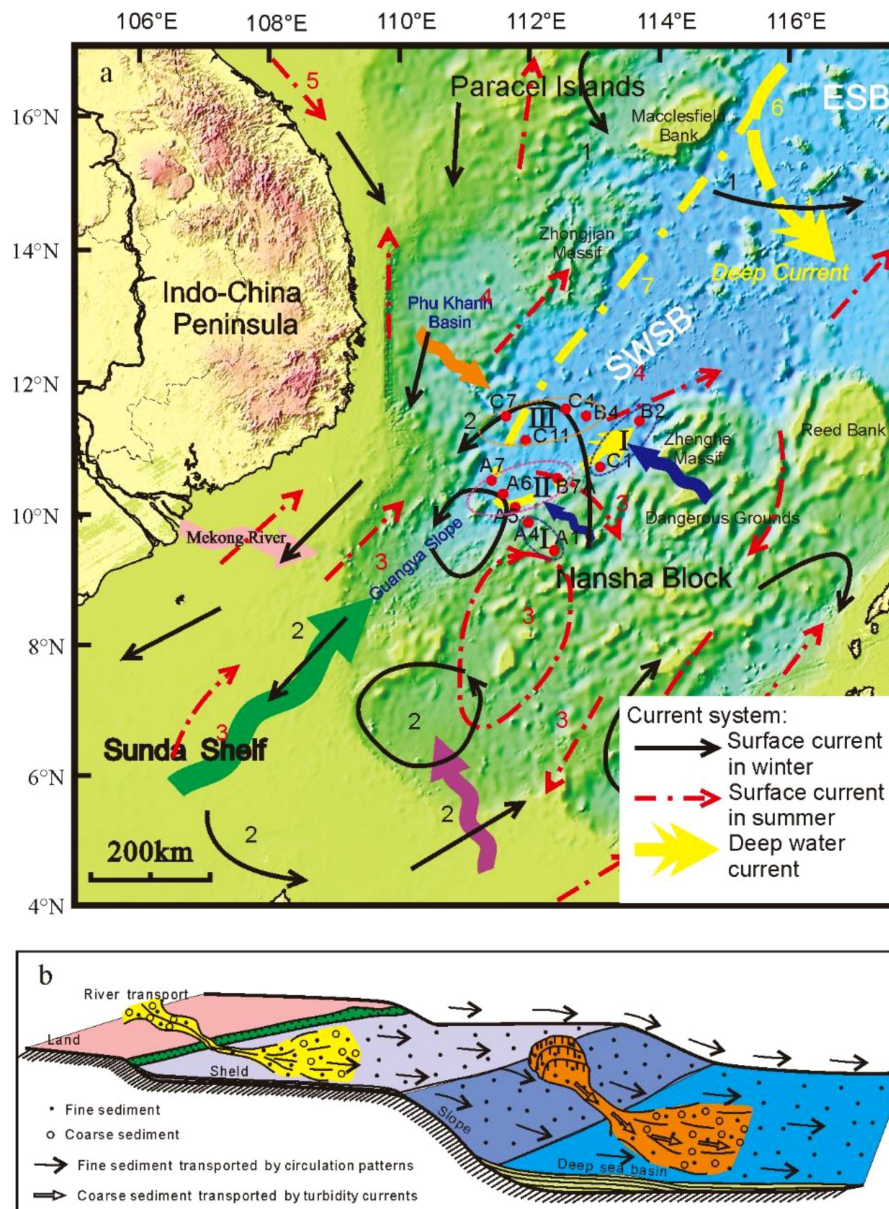


**FIGURE 11**  
 Model of sediment sources and transport pathways in the SWSB. **(A)** The dotted circles represent the regions divided according to different sources. The thick arrows represent sediment transport routes from the source areas to the deep basin. The arrow size represents the sediment contribution. The current systems are referenced from Liu et al. (2016) and Wang et al. (2018): 1, NW Luzon Cyclonic Gyre; 2, SCS Southern Cyclonic Gyre; 3, SCS Southern Anticyclonic Gyre; 4, SE Vietnam Offshore Current; 5, Gulf of Tonkin Surface Current; 6, Deep Cyclonic Current; and 7, SWSB Deep Cyclonic Current. **(B)** The section diagram of the deep-sea sediment sources and transport pathways. The deep-sea sediments are mainly terrigenous and were imported by rivers, the fine sediment was transported by circulation patterns, and the coarse sediment was transported by turbidity currents.

turbidity currents from the Guangya Slope in the southwest (Region II in Figure 11A), the Phu Khanh Basin in the north (Region III in Figure 11A) and the Nansha Block in the south (Region I in Figure 11A).

Based on the above analysis, we establish a transport model of deep-sea sediments in the SWSB of the South China Sea (Figure 11B). The deep-sea sediments are mainly terrigenous and have multiple sources. The transport of deep-sea sediments in the SWSB can be divided into two stages. In the first stage, terrigenous materials were transported by rivers and surface currents to the continental margin near the SWSB. In the second stage, the fine terrigenous materials of

the continental margin near the SWSB were transported to the deep-sea basin by circulation patterns, and the coarse terrigenous materials were transported to the deep-sea basin by turbidity currents.

## 6 Conclusions

Research on the sources and transport mechanisms of deep-sea sediments has always been limited by sample collection, and the same is true for this study. The cores collected from the SWSB are limited, and

the coverage is poor. Therefore, more tests cannot be performed, such as clay mineralogy, grain-size end-member component determination and dating. More work needs to be carried out in the future. Nonetheless, we obtain several meaningful insights:

- (1) The main minerals in the core sediments are quartz and feldspar, and turbidites are widely distributed in the SWSB.
- (2) The sediments within the SWSB are rich in terrestrial materials, which are derived from multiple sources, mainly including the Mekong River, Sunda Shelf and Red River.
- (3) A transport model of deep-sea sediments in the SWSB is preliminarily established. Terrigenous materials were first transported by rivers and surface currents to continental margins near the SWSB, and fine materials were subsequently transported by surface currents to the deep-sea basin, while coarse materials, especially turbidites, were transported by turbidity currents.

## Data availability statement

The datasets presented in this study can be found in online repositories. The names of the repository/repositories and accession number(s) can be found in the article/supplementary material.

## Author contributions

ZC: Conceptualization, Writing – original draft. XW: Data curation, Writing – review & editing. LZ: Conceptualization, Writing – original draft. CZ: Data curation, Writing – review & editing. XS: Data curation, Writing – review & editing.

## References

- Bao, R., Jia, G., and Zhang, C. (2019). Spatiotemporal variation of organic geochemical properties since the mid-Miocene in the deep South China Sea (IODP Expedition 349). *J. Asian Earth Sci.* 183, 103961. doi: 10.1016/j.jseas.2019.103961
- Boynton, W. V. (1984). Geochemistry of the Rare Earth Elements: Meteorite Studies. *Rare Earth Element Geochemistry*, Elsevier, 63–114.
- Cai, G. Q., Qiu, Y., Peng, X. C., and Zhong, H. X. (2010). The geochemical characteristics of trace elements and rees in surficial sediments of the Southwestern South China Sea and their implications. *Marine Geol. Quaternary Geol.* 30, 53–62. doi: 10.3724/SP.J.1140.2010.05053
- Cao, Y., Li, C. F., and Yao, Y. (2017). Thermal subsidence and sedimentary processes in the South China Sea Basin. *Mar. Geol.* 394, 30–38. doi: 10.1016/j.margeo.2017.07.022
- Chang, Y. T., Hsu, W. L., Tai, J. H., Tang, T. Y., Chang, M. H., and Chao, S. Y. (2010). Cold deep water in the South China Sea. *J. Oceanogr.* 66, 183–190. doi: 10.1007/s10872-010-0016-x
- Chen, F., Li, X., Liu, J., Lu, H., Wang, J., Zhang, X., et al. (2007). Characteristics of turbidity current deposits of core SA14-34 in deep sea basin of the Western South China Sea. *Geological Res. South China Sea*, 31–39. (in Chinese with English abstract)
- Chen, H., Qu, Y., and Zhong, H. (2004). Characteristics of grain size of core sediments in the southwest basin of South China Sea. *Geological South China Sea*, 66–74. (in Chinese with English abstract)
- Clark, M. K., House, M. A., Royden, L. H., Whipple, K. X., Burchfiel, B. C., Zhang, X., et al. (2005). Late Cenozoic uplift of southeastern Tibet. *Geology* 33, 525–528. doi: 10.1130/G21265.1
- Clift, P., Lee, G. H., Anh Duc, N., Barckhausen, U., Van Long, H., and Zhen, S. (2008). Seismic reflection evidence for a Dangerous Grounds miniplate: No extrusion origin for the South China Sea. *Tectonics* 27, TC3008. doi: 10.1029/2007TC002216
- Clift, P. D. (2006). Controls on the erosion of Cenozoic Asia and the flux of clastic sediment to the ocean. *Earth Planet. Sci. Lett.* 241, 571–580. doi: 10.1016/j.epsl.2005.11.028
- Clift, P. D., Wan, S., and Blusztajn, J. (2014). Reconstructing chemical weathering, physical erosion and monsoon intensity since 25Ma in the northern South China Sea: A review of competing proxies. *Earth-Sci. Rev.* 130, 86–102. doi: 10.1016/j.earscirev.2014.01.002
- Colin, C., Siani, G., Sicre, M. A., and Liu, Z. F. (2010). Impact of the East Asian monsoon rainfall changes on the erosion of the Mekong River basin over the past 25,000 yr. *Mar. Geol.* 271, 84–92.
- Ding, W., Franke, D., Li, J., and Steuer, S. (2013). Seismic stratigraphy and tectonic structure from a composite multi-channel seismic profile across the entire Dangerous Grounds, South China Sea. *Tectonophysics* 582, 162–176. doi: 10.1016/j.tecto.2012.09.026
- Fang, G., Fang, W., Yue, F., and Kai, W. (1998). A survey of studies on the South China Sea upper ocean circulation. *Acta Oceanographica Taiwanica* 37, 1–16.
- Fu, S. Q., Zhu, Z. Y., Ouyang, T. P., Qiu, Y., and Wei, Z. Q. (2011). Geochemical changes of the terrigenous sediments in the southern South China Sea and their paleoenvironmental implications during the last 31 ky. *J. Oceanogr.* 67, 337–346.
- Goldstein, S., and Jacobsen, S. (1988). Nd and Sr isotope systematics of river water suspended material - Implications for crustal evolution. *Earth Planet. Sci. Lett.* 87 (3Fe).

## Funding

The author(s) declare financial support was received for the research, authorship, and/or publication of this article. This work was supported by the National Natural Science Foundation of China (Grant No. 42176074). The cores were obtained from the Marine IV/HYIV20150816 survey cruise of the Guangzhou Marine Geological Survey. The major element, magnetic susceptibility and colours data were obtained from an X-ray fluorescence (XRF) core scanner at the Guangzhou Marine Geological Survey. The geochemical data were obtained from Nanjing FocuMS Technology Co., Ltd. The grain-size data were obtained from the School of Marine Science of Sun Yat-sen University, and the X-ray powder diffraction (XRD) data were obtained from the testing centre of Sun Yat-sen University.

## Conflict of interest

The authors declare that the research was conducted in the absence of any commercial or financial relationships that could be construed as a potential conflict of interest.

## Publisher's note

All claims expressed in this article are solely those of the authors and do not necessarily represent those of their affiliated organizations, or those of the publisher, the editors and the reviewers. Any product that may be evaluated in this article, or claim that may be made by its manufacturer, is not guaranteed or endorsed by the publisher.

- Hall, R. (2002). Cenozoic geological and plate tectonic evolution of SE Asia and the SW Pacific: computer-based reconstructions, model and animations. *J. Asian Earth Sci.* 20, 353–431. doi: 10.1016/S1367-9120(01)00069-4
- Haskin, M. A., and Haskin, L. A. (1984). Rare earths in European shales: A redetermination. *Science* 154, 507–509. doi: 10.1126/science.154.3748.507
- Hinz, K., and Schlüter, H. (1985). Geology of the Dangerous Grounds, South China Sea, and the continental margin off southwest Palawan: Results of SONNE cruises SO-23 and SO-27. *Energy* 10, 297–315. doi: 10.1016/0360-5442(85)90048-9
- Hiscott, R. N. (2001). Depositional sequences controlled by high rates of sediment supply, sea-level variations, and growth faulting: The Quaternary Baram Delta of northwestern Borneo. *Mar. Geol.* 175, 67–102. doi: 10.1016/S0025-3227(01)00118-9
- Huang, J., Jiang, F. Q., Wan, S. M., Zhang, J., Li, A. C., and Li, T. G. (2016). Terrigenous supplies variability over the past 22,000yr in the southern South China Sea slope: Relation to sea level and monsoon rainfall changes. *J. Asian Earth Sci.* 117, 317–327.
- Huang, J., Jiao, W. J., Liu, J. X., Wan, S. M., Xiong, Z. F., Zhang, J., et al. (2021). Sediment distribution and dispersal in the southern South China Sea: Evidence from clay minerals and magnetic properties. *Mar. Geol.* 439, 1–10. doi: 10.1016/j.margeo.2021.106560
- Jiwarungruangkul, T., and Liu, Z. F. (2021). East Asian monsoon and sea-level controls on clay mineral variations in the southern South China Sea since the Last Glacial Maximum. *Quaternary Int.* 592, 1–11. doi: 10.1016/j.quaint.2021.04.033
- Jiwarungruangkul, T., Liu, Z. F., Statterger, K., and Sang, P. N. (2019a). Reconstructing chemical weathering intensity in the Mekong River basin since the Last Glacial Maximum. *Paleoceanog. Paleoclimatol.* 34, 1710–1725. doi: 10.1029/2019PA003608
- Jiwarungruangkul, T., Liu, Z. F., and Zhao, Y. L. (2019b). Terrigenous sediment input responding to sea level change and East Asian monsoon evolution since the last deglaciation in the southern South China Sea. *Glob. Planet. Change* 174, 127–137. doi: 10.1016/j.gloplacha.2019.01.011
- Lei, C., Ren, J., Sternai, P., Fox, M., Willett, S., Xie, X., et al. (2015). Structure and sediment budget of Yinggehai–Song Hong basin, South China Sea: Implications for Cenozoic tectonics and river basin reorganization in Southeast Asia. *Tectonophysics* 655, 177–190. doi: 10.1016/j.tecto.2015.05.024
- Li, C. F., Xu, X., Lin, J., Sun, Z., Zhu, J., Yao, Y. J., et al. (2014). Ages and magnetic structures of the south China sea constrained by deep tow magnetic surveys and IODP expedition 349. *Geochem. Geophys. Geosys.* 15, 4958–4983. doi: 10.1002/2014GC005567
- Li, T., Li, X. J., Zhang, J. Y., Luo, W. D., Tian, C. J., and Zhao, L. (2020). Source identification and co-occurrence patterns of major elements in South China Sea sediments. *Mar. Geol.* 428, 106285. doi: 10.1016/j.margeo.2020.106285
- Liu, C., Clift, P. D., Murray, R. W., Blusztajn, J., Ireland, T., Wan, S. M., et al. (2017). Geochemical evidence for initiation of the modern Mekong Delta in the southwestern South China Sea after 8 Ma. *Chem. Geol.* 451, 38–54. doi: 10.1016/j.chemgeo.2017.01.008
- Liu, J., Chen, M., Chen, Z., and Yan, W. (2010a). Clay mineral distribution in surface sediments of the South China Sea and its significance for in sediment sources and transport. *Chin. J. Oceanol. Limnol.* 28, 407–415. doi: 10.1007/s00343-010-9057-7
- Liu, Z. F., Colin, C., Li, X. J., Zhao, Y. L., Tuo, S. T., Chen, Z., et al. (2010b). Clay mineral distribution in surface sediments of the northeastern South China Sea and surrounding fluvial drainage basins: Source and transport. *Mar. Geol.* 277, 48–60. doi: 10.1016/j.margeo.2010.08.010
- Liu, Z. F., Colin, C., Trentesaux, A., Blamart, D., Bassinot, F., Siani, G., et al. (2004). Erosional history of the eastern Tibetan Plateau over the past 190 kyr: clay mineralogical and geochemical investigations from the southwestern South China Sea. *Mar. Geol.* 209, 1–18. doi: 10.1016/j.margeo.2004.06.004
- Liu, Z. F., Colin, C., Trentesaux, A., Siani, G., Frank, N., Blamart, D., et al. (2005). Late Quaternary climatic control on erosion and weathering in the eastern Tibetan Plateau and the Mekong Basin. *Quat. Res.* 63, 316–328. doi: 10.1016/j.yqres.2005.02.005
- Liu, Z. F., Colin, C., Wei, H., Le, K. P., Tong, S. Q., Chen, Z., et al. (2007a). Climatic and tectonic controls on weathering in south China and IndoChina Peninsula: Clay mineralogical and geochemical investigations from the Pearl, Red, and Mekong drainage basins. *Geochem. Geophys. Geosys.* 8 (5), 1–18. doi: 10.1029/2006GC001490
- Liu, Z. F., Zhao, Y. L., Colin, C., Statterger, K., Wiesner, M. G., Huh, C.-A., et al. (2016). Source-to-sink transport processes of fluvial sediments in the South China Sea. *Earth-Sci. Rev.* 153, 238–273. doi: 10.1016/j.earscirev.2015.08.005
- Liu, Z. F., Zhao, Y. L., Li, J. R., and Colin, C. (2007b). Late Quaternary clay minerals off Middle Vietnam in the western South China Sea: Implications for source analysis and East Asian monsoon evolution. *Sci. China Ser. D: Earth Sci.* 50, 1674–1648. doi: 10.1007/s11430-007-0115-8
- Milliman, J. D., and Syvitski, J. P. M. (1992). Geomorphic/tectonic control of sediment discharge to the ocean: the importance of small mountainous rivers. *J. Geol.* 100, 525–544. doi: 10.1086/629606
- Qu, T. D. (2002). Evidence for water exchange between the South China Sea and the Pacific Ocean through the Luzon Strait. *Acta. Oceanologica Sinica* 21, 175–185.
- Qu, T. D., Girton, J. B., and Whitehead, J. A. (2006). Deepwater overflow through Luzon Strait. *J. Geophys. Res.* 111, C01002. doi: 10.1029/2005JC003139
- Schroeder, A., Wiesner, M. G., and Liu, Z. (2015). Fluxes of clay minerals in the South China Sea. *Earth Planet. Sci. Lett.* 430, 30–42. doi: 10.1016/j.epsl.2015.08.001
- Shao, L., Pang, X., Qiao, P., Chen, C., Li, Q., and Miao, W. (2008). Sedimentary filling of the Pearl River Mouth Basin and its response to the evolution of the Pearl River. *Acta Sedimentologica Sin.* 26, 179–185.
- Shaw, P.-T., and Chao, S.-Y. (1994). Surface circulation in the South China Sea. *Deep Sea Res. Part I: Oceanographic Res. Pap.* 41, 1663–1683. doi: 10.1016/0967-0637(94)90067-1
- Staub, J. R., Among, H. L., and Gastaldo, R. A. (2000). Seasonal sediment transport and deposition in the Rajang River delta, Sarawak, East Malaysia. *Sedimentary Geol.* 133, 249–264. doi: 10.1016/S0037-0738(00)00042-7
- Steinke, S., Chiu, H.-Y., Yu, P.-S., Shen, C.-C., Erlenkeuser, H., Löwemark, L., et al. (2006). On the influence of sea level and monsoon climate on the southern South China Sea freshwater budget over the last 22,000 years. *Quaternary Sci. Rev.* 25, 1475–1488. doi: 10.1016/j.quascirev.2005.12.008
- Steinke, S., Hanebuth, T. J. J., Vogt, C., and Statterger, K. (2008). Sea level induced variations in clay mineral composition in the southwestern South China Sea over the past 17,000 yr. *Mar. Geol.* 250, 199–210. doi: 10.1016/j.margeo.2008.01.005
- Su, D., White, N., and McKenzie, D. (1989). Extension and subsidence of the Pearl River mouth basin, northern South China Sea. *Basin Res.* 2, 205–222. doi: 10.1111/j.1365-2117.1989.tb00036.x
- Tong, S. Q. (2007). *Elemental geochemistry of surface sediments in the Pearl river, Red River and Mekong River(D)*, Tongji University of China: Master's thesis. (in Chinese with English abstract).
- Wan, S. M., Clift, P. D., Zhao, D. B., Hovius, N., Munhoven, G., France-Lanord, C., et al. (2017). Enhanced silicate weathering of tropical shelf sediments exposed during glacial lowstands: a sink for atmospheric CO<sub>2</sub>. *Geochim. Cosmochim. Acta* 200, 123–144. doi: 10.1016/j.gca.2016.12.010
- Wan, Z. F., Wang, X. Q., Li, Y. F., Xu, X., Sun, Y. F., Yin, Z. X., et al. (2019). The composition and geochemical significance of organic matters in surface sediments from the Southwest Sub-basin of the South China Sea. *J. Asian Earth Sci.* 171, 103–117. doi: 10.1016/j.jseaes.2018.07.012
- Wang, A. M., Du, Y., Peng, S. Q., Liu, K. X., and Huang, R. X. (2018). Deep water characteristics and circulation in the South China Sea. *Deep Sea Res. Part I: Oceanographic Res. Pap.* 134, 55–63. doi: 10.1016/j.dsr.2018.02.003
- Wang, G. H., Xie, S. P., Qu, T. D., and Huang, R. X. (2011). Deep South China Sea circulation. *Geophys. Res. Lett.* 38, 3115–3120. doi: 10.1029/2010GL046626
- Wang, P. X. (1999). Response of Western Pacific marginal seas to glacial cycles: paleoceanographic and sedimentological features 1. *Mar. Geol.* 156, 5–39. doi: 10.1016/S0025-3227(98)00172-8
- Wang, P. X., and Li, Q. Y. (2009). *The South China Sea: Paleoceanography and Sedimentology Development in Palaeoenvironmental Research* Vol. 13 (Germany: Springer), 506 pp.
- Wei, G. J., Liu, Y., Li, X. H., Chen, M. H., and Wei, W. C. (2003a). High-resolution elemental records from the South China Sea and their paleoproductivity implications. *Paleoceanography* 18, 1054. doi: 10.1029/2002PA000826
- Wei, G. J., Liu, Y., Li, X. H., Liang, X. R., and Shao, L. (2003b). Excess al in the sediments from South China Sea. *Bull. Mineral. Petrol. Geochem.* 22, 23–25. doi: 10.0000/j.issn.1007-2802.2003.22.10318
- Wei, G. J., Liu, Y., Ma, J. L., Xie, L. H., Chen, J. F., Deng, W. F., et al. (2012). Nd, Sr isotopes and elemental geochemistry of surface sediments from the South China Sea: Implications for Provenance Tracing. *Mar. Geol.* 319–322, 21–34.
- Wu, Y. M., Ding, W. W., Sun, Z., Dong, C. Z., and Fang, Y. X. (2018). Sedimentary budget of the Southwest Sub-basin, South China Sea: Controlling factors and geological implications. *Geological J.* 53, 3082–3092. doi: 10.1002/gj.3145
- Wyrtki, K. (1961). *Physical oceanography of the southeastern Asia waters. scientific results of marine investigations of the South China Sea and gulf of Thailand*, 1959–1961. Naga Report, 2.
- Yin, Z. X., Cai, Z. R., Zhang, C., Huang, X. F., Huang, Q. R., and Chen, L. (2021). Tectonic unit divisions based on block tectonics theory in the South China Sea and its adjacent areas. *Acta Oceanologica Sinica* 40, 33–42. doi: 10.1007/s13131-021-1898-8
- Zhang, L. L., Chen, M. H., Chen, Z., Xiang, R., and Liu, J. G. (2010). Distribution of calcium carbonate and its controlling factors in surface sediments of the South China Sea. *Earth Sci.* 35, 891–898. doi: 10.3799/dqkx.2010.104
- Zhao, Y. L., Liu, Z. F., Colin, C., Xie, X., and Wu, Q. (2011). Turbidite deposition in the southern South China Sea during the last glacial: Evidence from grain-size and major elements records. *Chin. Sci. Bull.* 56, 3558–3565. doi: 10.1007/s11434-011-4685-7